Substrate-Induced Photofield Effect in Graphene Phototransistors

Nauman Z. Butt, *Member, IEEE*, Biddut K. Sarker, Yong P. Chen, *Member, IEEE*, and Muhammad Ashraful Alam, *Fellow, IEEE*

***Abstract*— A single atomic layer of graphene, integrated onto an undoped bulk substrate in a back-gated transistor configuration, demonstrates surprising strong photoconduction, and yet, the physical origin of the photoresponse is not fully understood. Here, we use a detailed computational model to demonstrate that the photoconductivity arises from the electrostatic doping of graphene, induced by the surface accumulation of photogenerated carriers at the graphene/substrate interface. The accumulated charge density depends strongly on the rate of charge transfer between the substrate and the graphene; the suppression of the transfer rate below that of carrier's thermal velocity is an essential prerequisite for a substantial photoinduced doping in the graphene channel under this mechanism. The contact-to-graphene coupling (defined by the ratio of graphene–metal contact capacitance to graphene's quantum capacitance) determines the magnitude of photoinduced doping in graphene at the source/drain contacts. High-performance graphene phototransistors would, therefore, require careful engineering of the graphene–substrate interface and optimization of graphene–metal contacts.**

***Index Terms*— Electrostatic doping, graphene, photodetector, phototransistor.**

I. Introduction

GRAPHENE is composed of a single layer of carbon atoms, which are arranged in a hexagonal crystalline form. The material possesses remarkable electrical, optical, and mechanical properties, making it attractive for a broad spectrum of nanoelectronic and photonic devices [1]–[3]. Ever since the first experimental demonstration of monolayer graphene in 2004 [4], it has found innovative applications in a variety of devices appropriate for microprocessors, displays, sensors, and optoelectronics/photonics [5]–[8]. Among these, graphene-based photodetectors and phototransistors have recently attracted considerable attention as broadband, high-performance, highly reliable, and (potentially) low-cost alternatives to traditional devices. A variety of device configurations have been explored: some configurations offer ultrahigh-speed switching, while others target highly sensitive response [8]–[15]. In general, the device has a back-gated FET structure, in which graphene forms the transport layer on the top of either a semiconductor substrate or a dielectric.

Based on the performance parameters and the dominant physical mechanism, graphene-based photodetectors could broadly be divided into two categories: 1) Type-1 devices rely on photoabsorption in graphene and the photocurrent is attributed to the combination of photovoltaic, photothermoelectric, and bolometric responses of graphene itself. The substrates in these devices do not contribute to the photoresponse. These devices have demonstrated a very high speed (in the range of gigahertz); their photoresponsivity has, however, been relatively low (in the range of milliampere/watt) [9]. A number of design approaches are being explored to improve the photoresponsivity of Type-1 photodetectors, e.g., by integrating various innovative receptors, such as plasmonic nanostructures, quantum dots, microcavities, and trap centers, and through band engineering [13], [16]–[20]. 2) The second configuration (Type-II) of graphene-based photodetection involves a phototransistor that is composed of a graphene channel integrated on the top of an undoped semiconductor substrate. In these devices, the undoped semiconductor substrate acts as the light absorber, and the photogenerated charge carriers in the substrate (rather than in graphene) play the dominant role in photodetection [21]–[24]. These devices have shown a very high photoresponsivity up to few amperes per watt. The photodetection mechanism in Type-II devices has been attributed to the conductivity modulation of graphene as the photogenerated carriers in the substrate modulate the electric field at the graphene/substrate interface [21], [23], [24]. Such a photodetection mechanism has not been treated by rigorous, self-consistent theoretical models; as a result, the principle of device operation and the origin of extremely high photoconduction are not fully understood.

Here, we present a computational model that explains the essential physics of a series of experimental observations and develops an intuitive understanding of the device operation. In particular, we address the following key questions in Type-II graphene phototransistors.

1) What is the origin of surprisingly high photoresponse?

Manuscript received July 2, 2015; revised August 13, 2015; accepted August 27, 2015. Date of current version October 20, 2015. The review of this paper was arranged by Editor J. Huang.

N. Z. Butt is with the Department of Electrical Engineering, Syed Babar Ali School of Science and Engineering, Lahore University of Management Sciences, Lahore 54792, Pakistan (e-mail: nauman.butt@lums.edu.pk).

B. K. Sarker is with the Department of Physics and Astronomy, Purdue University, West Lafayette, Indiana 47907 USA (e-mail: bsarker@purdue.edu).

Y. P. Chen is with the Department of Physics and Astronomy, Purdue University, West Lafayette, IN 47907 USA (e-mail: yongchen@purdue.edu).

M. A. Alam is with the School of Electrical and Computer Engineering, Purdue University, West Lafayette, IN 47907 USA (e-mail: alam@purdue.edu).

Color versions of one or more of the figures in this paper are available online at http://ieeexplore.ieee.org.

Digital Object Identifier 10.1109/TED.2015.2475643

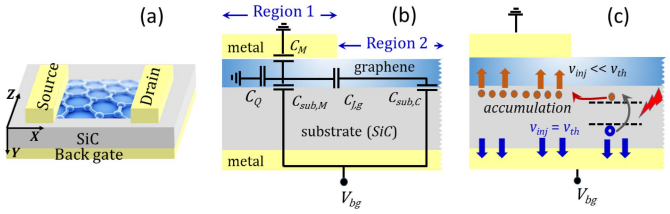

Fig. 1. (a) Graphene field-effect phototransistor. A single-layer graphene forms the channel between the source/drain metal contacts. An undoped semiconductor substrate (SiC in our model) acts as the photoabsorber, which modulates graphene conductivity through electrostatic coupling. A back-gate voltage ($V_{\rm bg}$) provides an electric field in the substrate for photogenerated charge separation. (b) Capacitance model for the graphene phototransistor. The cross section for one-half of the device is shown. (c) Photogenerated carrier transport. A drift-diffusion model describes the carrier transport in the substrate, where the carriers are injected into the graphene with velocity ($v_{\rm inj}$).

2) What material/structural knobs are available to optimize the photoresponse?
3) How does the photoresponse depend on the incident light intensity?
4) What is the origin of symmetrical vs. asymmetrical response of the ambipolar photoconduction?

The remainder of this paper is organized as follows. Section II presents our theoretical approach. The results are discussed in Section III. The conclusions are provided in Section IV.

II. Theoretical Approach

A. Model System

An illustration of the investigated device is shown in Fig. 1(a). The structure is a field-effect phototransistor, in which graphene forms the channel that is back gated through an intrinsic (undoped) silicon carbide (6H–SiC) substrate and is contacted at the top by source/drain metal. The model is independent from any specific process/deposition method of graphene. The interfacial properties (such as the binding energy) of graphene with the substrate/metal, which might be process dependent, are treated in a generalized approach. To elaborate our model system, we divide the device cross section into two regions, as highlighted in Fig. 1(b). Region 1 defines the cross section under the metal contacts, whereas the cross section under the channel is defined by Region 2. Under illumination, we anticipate uniform photogeneration throughout the device.

B. Electrostatic Model

A quantitative model for electrostatics is implemented by the numerical solution of 2-D Poisson equation [see (A1) in the Appendix], which includes the effect of applied voltages and the photogenerated charges in the substrate. A qualitative understanding can, however, be developed using a simple capacitance model, as shown in Fig. 1(b). The device cross section highlights various capacitances that could affect the electrostatics of graphene. $C_{{\rm sub},M}$ and $C_{{\rm sub},C}$ define the graphene-to-substrate capacitances in Region 1 and Region 2, respectively. The capacitance C_Q represents the quantum capacitance in graphene, and the capacitance $C_{J,g}$ represents the junction capacitance between Region 1 and Region 2 in graphene if the regions differ in photoinduced electrostatic doping. The electrostatic coupling of graphene with the metal at the source/drain contacts is represented by C_M. The nature of metal–graphene interfacial chemical bonding, especially for different types of deposition conditions, is not fully understood. If the bonding is weak and the contact is nonohmic, as suggested in [25] and [26], then the interface can be modeled by a thin interfacial dielectric layer between the metal and the underlying graphene, resulting in a finite C_M. In this formulation, an ohmic contact between the graphene–metal will be described by $C_M \to \infty$. Note that the electrostatic doping of graphene in Region 1 depends on the relative magnitude of C_M and C_Q: with respect to this, there could be two limiting scenarios: 1) For $C_M \to \infty$, the graphene's potential, i.e., Dirac point energy (E_D) in Region 1 would be completely controlled by the potential of the metal contact, and electrostatic doping of Region 1 would be impossible. 2) If, on the other hand, an interfacial dielectric barrier exists between the metal and the graphene, the limiting case could be $C_M \ll C_Q$. E_D for graphene in Region 1 under this limit would experience the maximum effect of quantum capacitance provided that there is a substantial field effect induced by the density of photogenerated carriers at the SiC surface under the source/drain contacts. Away from the source/drain contacts in Region 2, the electrostatic effects of the contacts are fully screened; therefore, E_D floats with the surface potential of the substrate (here SiC). The photoinduced doping of Region 2, therefore, depends on the modulation of the surface potential in SiC underneath the channel.

C. Transport Model

To model the charge transport in graphene–SiC field-effect phototransistor, we consider two distinct components of the photogenerated carrier transport, as shown in Fig. 1(c). The first component is the semiclassical transport of photogenerated carriers in SiC which requires the solution of the drift-diffusion equation. The second component is the quantum mechanical charge transfer from the SiC into the graphene. To incorporate both of these transport components in a single computational model, we have adopted a phenomenological approach, in which graphene is treated as an electrode and the carrier transfer flux at the graphene/SiC interface provides a boundary condition to the solution of the drift-diffusion transport in SiC [see (A2) and (A3) in the Appendix]. To model the quantum mechanical carrier transfer flux between the SiC and the graphene, we calculate the velocity ($v_{\rm inj}$) of carrier injection from the SiC into the graphene that depends on the rate of carrier transfer at the SiC/graphene interface. For a standard metal/semiconductor Schottky contact, $v_{\rm inj}$ is approximately equal to the carrier's thermal velocity ($v_{\rm th}$) which depends only on the temperature and bandstructure of the semiconductor. Recent experimental data [24] on graphene phototransistors integrated on the SiC substrate have, however, indicated the presence of a thin

TABLE I
CALCULATION OF INJECTION VELOCITY *

t_{ox} (A)	$v_{th,elec}$ (cm/s)	$v_{th,hole}$ (cm/s)	ϕ_{elec} (eV)	ϕ_{hole} (eV)	$v_{inj,elec}$ (cm/s)	$v_{inj,hole}$ (cm/s)
1	1.5×10^{3}	1.2×10^{3}	2.4	3.5	3.2×10^{2}	1.8×10^{2}
3	1.5×10^{3}	1.2×10^{3}	2.4	3.5	1.4×10^{1}	4.4×10^{0}
5	1.5×10^{3}	1.2×10^{3}	2.4	3.5	6.5×10^{-1}	1.0×10^{-1}
7	1.5×10^{3}	1.2×10^{3}	2.4	3.5	2.9×10^{-2}	2.5×10^{-3}
10	1.5×10^{3}	1.2×10^{3}	2.4	3.5	2.8×10^{-4}	9.0×10^{-6}

*t_{ox} refers to SiO_2 thickness between graphene and SiC, $v_{th,elec}$ ($v_{th,hole}$) are thermal velocities in SiC, ϕ_{elec} (ϕ_{hole}) are energy barrier height at SiC/SiO_2 interface, $v_{inj,elec}$ ($v_{inj,hole}$) are the injection velocity at graphene/SiC interface for electrons (holes) .

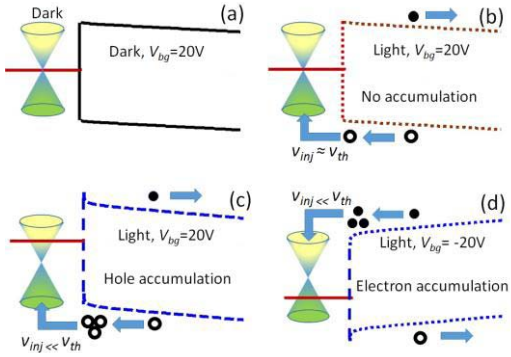

Fig. 2. Energy band diagram near the graphene/substrate interface in Region 1 (a) in dark and (b)–(d) under illumination. No electrostatic doping in graphene is observed in dark. In (b), photogenerated carriers do not accumulate at the graphene/SiC interface, since $v_{\rm inj} \approx v_{\rm th}$, and hence no electrostatic doping in graphene. In (c) and (d), photogenerated holes and electrons, respectively, accumulate near the graphene/SiC interface (underneath the energy barrier, not drawn for simplicity) due to $v_{\rm inj} \ll v_{\rm th}$ for $V_{\rm bg} = 20$ V and $V_{\rm bg} = -20$ V, respectively. Graphene is doped n-type in (c) and p-type in (d), and $C_M \ll C_Q$ is assumed.

interfacial barrier at the graphene/SiC interface. It has been reported that a native oxide layer often forms naturally on the SiC surface [24], [27], [28] that could act as an energy barrier to the carriers at the graphene/SiC interface. An effective energy barrier at the interface may also exist due to a relatively weak chemical bonding between the graphene and the SiC as compared with a bulk Schottky junction [26]. The presence of an energy barrier at the graphene/SiC interface results in $v_{\rm inj} \ll v_{\rm th}$, which now becomes a function of thickness and height of the interfacial barrier. An estimate of $v_{\rm inj}$ in the presence of an interfacial oxide could be calculated analytically using Wentzel–Kramers–Brillouin approximation for tunneling through a rectangular energy barrier [29]

$$v_{\rm inj} = v_{\rm th} e^{-\beta\sqrt{\varphi} t_{\rm ox}} \tag{1}$$

where $t_{\rm ox}$ is the interfacial barrier thickness and given in Å, β is the tunneling constant, and φ is the energy barrier height in electron volts. The calculated $v_{\rm inj}$ from (1), assuming a thin SiO_2 layer at the graphene/SiC interface, is tabulated in the Appendix (Table I). A rigorous approach to model the charge transport through the semiconductor/graphene interface would require quantum mechanical models, e.g., the nonequilibrium Green function formalism [30], which are beyond the scope of this paper. Our approach is nevertheless appropriate for the phenomenological understanding of the physics of conductivity modulation in graphene and for qualitatively defining a design space for graphene-based phototransistors.

III. RESULTS AND DISCUSSION

A. Origin of High Photoresponsivity

Fig. 2 qualitatively shows the phenomenon of the photoinduced doping of graphene due to the field effect from the substrate. The energy band diagrams drawn at the SiC/graphene interface along the direction perpendicular to the channel in Region 1 with the illustrated surface charge density in SiC are shown for various limits of $v_{\rm inj}$ under dark and illumination. When the carriers are photogenerated in SiC under illumination, holes drift toward the source/drain contacts due to the applied gate voltage ($V_{\rm bg} = 20$ V). For the case when no interfacial barrier exists at the graphene/SiC interface, $v_{\rm inj} \approx v_{\rm th}$, and there is no accumulation of holes at the interface. Under this situation, there is no significant space charge present at the graphene/SiC interface, and hence there is negligible substrate-induced electrostatic effect in the graphene, as shown in Fig. 2(b). In the presence of an energy barrier at the interface ($v_{\rm inj} \ll v_{\rm th}$), the drift flux of photogenerated carriers flowing from the substrate results in charge accumulation near the SiC surface (underneath the barrier) in Region 1. The magnitude of the surface accumulation density in Region 1 develops such that it maintains the self-consistency between the steady-state photogenerated carrier flux drifting from the bulk and the surface carrier flux being injected into the metal contacts. This accumulated space charge near the graphene/SiC interface (more precisely at the interface between the SiC and the energy barrier which is not drawn for simplicity) could be significant enough to electrostatically doped graphene, as shown in Fig. 2(c) and (d).

The net charge concentration at the SiC surface (underneath graphene) along the channel direction (X) and along the direction (y) perpendicular to the channel (into the SiC) obtained from the numerical simulations are shown in Fig. 3(a) and (b), respectively, for $v_{\rm inj} = 10^{-3}$ cm/s, both under dark and illumination. Assuming an SiO_2 barrier, $v_{\rm inj} = 10^{-3}$ cm/s corresponds to $t_{\rm ox} \approx 7$ Å (see Table I) and is much smaller than $v_{\rm th} \approx 10^{3}$ cm/s for carriers in intrinsic SiC [31]. The maximum charge density under illumination is found to be at the SiC surface in Region 1 due to the surface accumulation of the photogenerated carriers that drift from the substrate toward the contact. The photogenerated charge density decreases exponentially while going away from the SiC surface in Region 1, both laterally into Region 2 [Fig. 3(a) (solid line)] and perpendicularly into the SiC thickness in Region 1 [Fig. 3(b) (dashed line)]. It should be noted that for $V_{\rm bg} = 0$ V, there is no surface accumulation, since the charge carriers generated in the field-free substrate recombine before reaching to the SiC

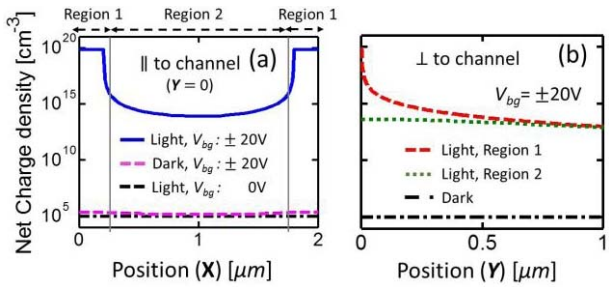

Fig. 3. Net charge density at the SiC surface underneath the energy barrier below the graphene/SiC interface along (a) channel direction and (b) direction perpendicular to the channel in dark and under illumination for $v_{\text{inj}} = 10^{-3}$ cm/s. The photogenerated carriers accumulate at the SiC surface in Region 1 for $v_{\text{inj}} \ll v_{\text{th}}$ and $V_{\text{bg}} = \pm 20$ V under illumination. For $V_{\text{bg}} = 0$ V and in dark, no photogenerated charge accumulation occurs. Vertical solid line in (a): boundaries of Regions 1 and Region 2. The back gate is at $Y = 500$ μm and the incident light power density (P_{inc}) = 18 mW/cm^2.

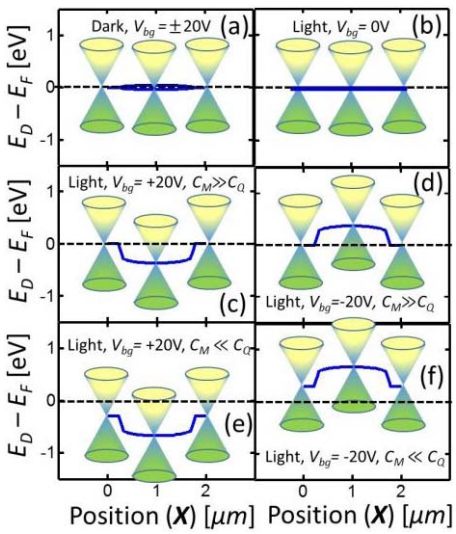

Fig. 4. (a)–(f) Substrate-induced electrostatic shift in Dirac energy (E_D) versus Fermi level (E_F) of graphene along the channel. v_{inj} is kept equal to 10^{-3} cm/s in (a)–(f). For (a) dark, an insignificant shift in ($E_D - E_F$) is due to the small electrostatic effect of V_{bg} on graphene. (b) Under illumination at $V_{\text{bg}} = 0$ V, photogenerated carriers recombine before they could reach to the contacts. Holes and electrons accumulate at the SiC surface in Region 1 under illumination for (c) and (e) $V_{\text{bg}} = +20$ V and (d) and (f) $V_{\text{bg}} = -20$ V, respectively. For (c) and (d) $C_M \gg C_Q$, E_D in graphene under metal remains fixed at the potential at the metal contact. The surface carrier accumulation in Region 1 electrostatically doped graphene channel (c) n-type for $V_{\text{bg}} = +20$ V and (d) p-type for $V_{\text{bg}} = -20$ V. For (e) and (f) $C_M \ll C_Q$, graphene in Region 1 also gets electrostatically doped.

surface [Fig. 3(a) (dashed line)]. As a result, the charge density for this case remains equal to that in the dark [Fig. 3(a) and (b) (dashed-dotted lines)]. In Region 2, the density of photogenerated carriers at the SiC surface [Fig. 3(b) (dotted line)] is significantly lower than that in Region 1 (carrier accumulation in Region 2 is insignificant), since the lateral flow of the drift current toward the source/drain contacts prevents any substantial accumulation of carriers in Region 2.

The photogenerated carrier accumulation at the SiC surface due to weak injection velocity of carriers into the source/drain contacts self-consistently enhances the lateral electric field and the potential drop between Region 1 and Region 2 along the SiC surface. The polarity and the magnitude of this modulation in the surface potential depend on the polarity (n or p) and the density of the accumulated charge carriers at the surface, respectively. The lateral modulation of the surface potential in Region 2 results in an electrostatic doping of graphene in the channel region, as shown in Fig. 4, for both the dark and under illumination. Under dark or at zero-gate voltage ($V_{\text{bg}} = 0$ V), no electrostatic doping is observed, as expected [Fig. 4(a) and (b) respectively]. For a finite-gate voltage ($V_{\text{bg}} = \pm 20$ V) and under illumination, only the channel region is electrostatically doped if $C_M \gg C_Q$ [Fig. 4(c) and (d)], whereas both the channel and the source/drain regions are electrostatically doped if $C_M \ll C_Q$ [Fig. 4(e) and (f)].

B. Dependence of Photoresponse on Device Parameters

Physical properties of the device, in particular, the interface of graphene with the source/drain metal and the substrate, which influence C_M and v_{inj}, respectively, strongly affect the photoresponse. The effect of relative magnitudes of C_Q and C_M on $E_D - E_F$ for graphene under the source/drain metal (Region 1) and in the channel (Region 2) are shown in Fig. 5(a) for $V_{\text{bg}} = \pm 20$ V, $v_{\text{inj}} = 10^{-3}$ cm/s, and incident power density of illumination (P_{inc}) of 18 mW/cm^2. The accumulated density of the photogenerated carriers at the SiC surface remains essentially unchanged with the modulation of C_M/C_Q, however the electrostatic doping of graphene in Region 1 and Region 2 varies with the magnitude of C_M/C_Q.

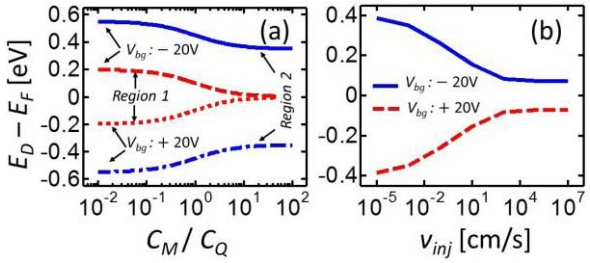

Fig. 5. (a) Shift in E_D for graphene under metal (Region 1) and in the channel (Region 2) as a function of C_M/C_Q for $V_{\text{bg}} = \pm 20$ V, $v_{\text{inj}} = 10^{-3}$ cm/s, and $P_{\text{inc}} = 18$ mW/cm^2. For $C_M/C_Q \ll 1$, the shift in E_D is maximum, which gradually reduces as C_M/C_Q is increased. For $C_M/C_Q \gg 1$, there is essentially no shift in E_D in Region 1, since the potential is completely controlled by the voltage of the metal contact. (b) Shift in E_D for graphene in the channel region as a function of v_{inj} for $V_{\text{bg}} = \pm 20$ V, $P_{\text{inc}} = 18$ mW/cm^2, and $C_M/C_Q \gg 1$. The shift in E_D increases for $v_{\text{inj}} < 10^3$ cm/s due to the increase in the accumulation of photogenerated carriers at the SiC surface. For $v_{\text{inj}} > 10^3$ cm/s, the effect of photoinduced doping is negligible, and the residual small shift in E_D is due to the effect of V_{bg}.

The two limiting cases, i.e., $C_M/C_Q \ll 1$ and $C_M/C_Q \gg 1$, correspond to the maximum possible electrostatic doping and the minimum doping in the graphene, respectively, for given values of P_{inc} and v_{inj}. When $C_M/C_Q \ll 1$, E_D in Region 1 is relatively independent of the potential of the source/drain metal and the photogenerated carrier accumulation at the SiC surface in Region 1 induces an electrostatic doping in the graphene under the source/drain metal through the effect of quantum capacitance ($E_D - E_F = qN_{\text{int}}/C_Q$), where N_{int} is the integrated charge density at the SiC surface in Region 1.

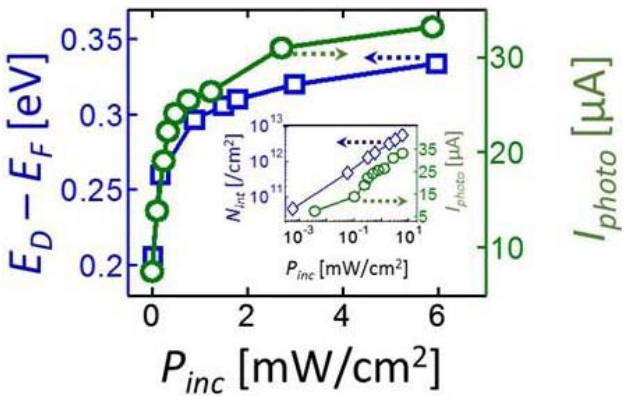

Fig. 6. Shift in E_D for graphene in the channel region as a function of P_{inc} for $v_{\text{inj}} = 10^{-3}$ cm/s, $V_{\text{bg}} = 20$ V, and $C_M/C_Q \gg 1$. The experimental photocurrent (I_{photo}) versus P_{inc} taken from [24] follows a similar trend. Inset: dependence of experimental I_{photo} and the surface charge density in SiC (integrated over the y-direction) on log (P_{inc}).

For $C_M/C_Q \gg 1$, there is essentially no shift in E_D in Region 1, since the graphene potential in Region 1 in this case is completely controlled by the voltage of the source/drain metal contacts. It should be noted that the shift in E_D in Region 1 as a function of C_M/C_Q also modulates the graphene potential in Region 2, as shown in Fig. 5(a).

Fig. 5(b) shows the effect of v_{inj} on electrostatic doping of graphene in the channel for $V_{\text{bg}} = \pm 20$ V, $C_M/C_Q \gg 1$, and a fixed incident power ($P_{\text{inc}} = 18$ mW/cm^2). As v_{inj} increases, charge accumulation density at the surface reduces, which lowers the electrostatic doping (smaller $E_D - E_F$). It is worth noting that $E_D - E_F$ starts showing a significant increase as v_{inj} is reduced below 10^3 cm/s. As shown in Table A1, this corresponds to the presence of an ultrathin energy barrier between the surface of SiC and graphene. For $v_{\text{inj}} > 10^3$ cm/s, the effect of photoinduced doping is negligible. The small shift in E_D observed for $v_{\text{inj}} > 10^3$ cm/s in Fig. 5(b) is due to the residual effect of V_{bg}, which remains independent of v_{inj}.

C. Dependence of Photoresponse on Input Light Intensity

The dependence of graphene's electrostatic doping in the channel on P_{inc} is shown in Fig. 6 at $V_{\text{bg}} = 20$ V and $v_{\text{inj}} = 10^{-3}$ cm/s. The photoresponse is maximum at lower P_{inc} and gradually flattens out at higher P_{inc}. This trend is qualitatively similar to the experimental observation of photocurrent (I_{photo}) versus P_{inc} [24], which is plotted in Fig. 6 for comparison. As P_{inc} is increased, the charge accumulation density at the SiC/graphene increases [shown in Fig. 6 (inset)], hence increasing the photoinduced doping in graphene. As the charge accumulation density increases, the subsequent flow of photogenerated carriers toward the SiC surface becomes slower which results in a gradual flattening of the response of $E_D - E_F$ and I_{photo} as a function of P_{inc}. This is expected since the higher accumulation of carriers at the SiC surface could result in a back-diffusion of carrier flux from the surface toward the substrate's bulk which opposes the photogenerated carrier flux drifting from the bulk toward the surface. In addition, the electric field in SiC bulk is reduced due to high carrier accumulation at the surface which could reduce the collection of photogenerated carriers from the bulk at the surface.

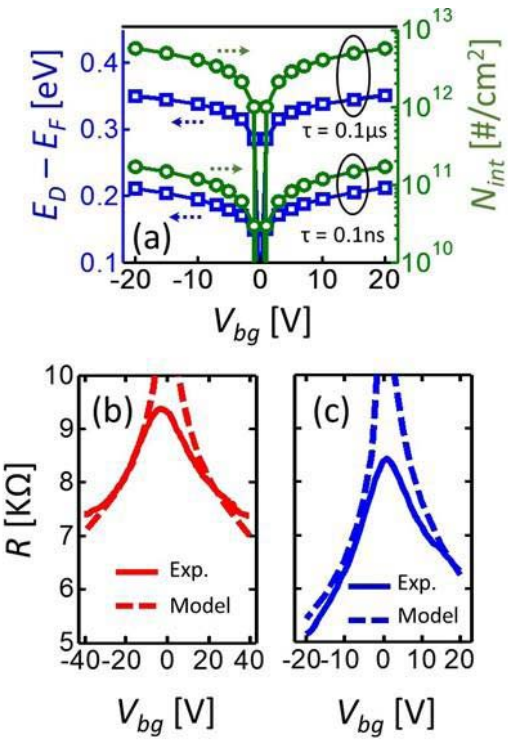

Fig. 7. (a) Magnitude of shift in E_D for graphene in the channel region and the integrated surface charge (N_{int}) in SiC under the source/drain contact (Region 1) as a function of V_{bg} for $v_{\text{inj}} = 10^{-3}$ cm/s, $P_{\text{inc}} = 18$ mW/cm^2, and $C_M/C_Q \gg 1$. N_{int} is due to the surface accumulation of holes (electrons) for the positive (negative) polarity of V_{bg}. The results are shown for two different carrier lifetimes (assumed the same for electrons and holes) in SiC. (b) Experimental back-gate-voltage modulation of graphene resistance ($R - V_{\text{bg}}$) in a graphene phototransistor with channel dimensions of $W \times L = 3\ \mu\text{m} \times 2\ \mu\text{m}$ under visible light illumination ($P_{\text{inc}} \approx 40$ mW/cm^2) is compared with the simulated $R - V_{\text{bg}}$. For the simulated result, the same injection velocity ($v_{\text{inj}} = 10^{-3}$cm/s) for electron and holes is used that shows a good match with the experimental ambipolar symmetric $R - V_{\text{bg}}$ characteristics. (c) Simulated $R - V_{\text{bg}}$ is compared with the experimental data from [23]. The experimental data are for a graphene phototransistor with channel dimensions of $W \times L = 4\ \mu\text{m} \times 1\ \mu\text{m}$ under visible light illumination ($P_{\text{inc}} \approx 7$ mW/cm^2). Different injection velocities ($v_{\text{inj}} = 5 \times 10^{-2}$ cm/s and $v_{\text{inj}} = 10^{-1}$cm/s for the electrons and holes, respectively) are assumed at the graphene/SiC interface in the simulated result. The simulation results in (b) and (c) are calculated from (2), where $C_M/C_Q \gg 1$ is assumed.

D. Origin of Symmetric/Asymmetric Ambipolar Photoconductivity

The ambipolar photoconduction in graphene phototransistors could have either symmetric or asymmetric dependence on the polarity of V_{bg}, as observed in the experiments [23], [24]. To understand the origin of this dependence, we explore the gate-voltage dependence of $E_D - E_F$ in the graphene channel region and that of the integrated photoinduced charge density accumulated at the SiC surface. Fig. 7 (a) shows these results for $P_{\text{inc}} = 18$ mW/cm^2 and $v_{\text{inj}} = 10^{-3}$ cm/s. The integrated surface charge density and $E_D - E_F$ show a similar trend, i.e., an ambipolar increase with increasing magnitude of V_{bg}. This is expected because at higher V_{bg}, the electric field across

substrate's thickness increases which enhances the drift length for the photogenerated carriers in the substrate. This results in an enhanced photogenerated carrier flux and the corresponding higher accumulated carrier density which increases the electrostatic doping in graphene as $V_{\rm bg}$ is increased. As the polarity of $V_{\rm bg}$ is reversed, the type (electron or hole) of the carriers accumulating at the SiC/graphene interface is switched, and the graphene is correspondingly doped (p or n) hence resulting into a symmetric ambipolar photoconduction. Fig. 7(a) also shows the relative importance of carrier lifetime (τ) in the SiC on the electrostatic doping of graphene. In general, carrier lifetime for crystalline 6H – SiC is reported in the range 0.1 ns – 0.1 μs [32], where a high-quality and pure SiC substrate is characterized by a relatively longer lifetime ($\tau = 0.1$ μs), while a lower quality and highly defective SiC substrate is best described by much shorter lifetime ($\tau = 0.1$ ns). Longer carrier lifetime increases the drift length of the carriers, and thereby increases the density of accumulated photogenerated carriers at the SiC surface. The corresponding electrostatic doping in the graphene is somewhat higher for $\tau = 0.1$ μs as compared with $\tau = 0.1$ ns, although the qualitative trend remains the same.

Fig. 7(b) and (c) compare the experimental photoinduced gate-voltage modulation of graphene resistance (R), i.e., the $R - V_{\rm bg}$ characteristics of graphene/SiC phototransistor, with the simulated $R - V_{\rm bg}$. The experimental data shown in Fig. 7(b) was measured on a device with channel dimensions of $W \times L = 3$ μm $\times$ 2 μm, where the whole sample was exposed under a visible light at an estimated $P_{\rm inc} \approx 40$ mW/cm^2. The fabrication and characterization of this device are similar to what are discussed in [24]. The experimental data in Fig. 7(c) are taken from [23] on a device with $W \times L = 4$ μm $\times 1 \mu$m under visible light illumination at an estimated $P_{\rm inc} \approx 7$ mW/cm^2. The calculated resistances are obtained assuming the low bias model for diffusive transport in graphene [33]

$$R = \alpha \left[\left(\frac{2e^2}{h} \right) \frac{\lambda}{L} \frac{2W}{\pi \hbar v_F} (\kappa_B T)(s+1) \Gamma(s+1)(\mathrm{F}_s(\eta_F) + \mathrm{F}_s(-\eta_F)) \right]^{-1} \quad (2)$$

where Γ is the gamma function, F_s is the Fermi–Dirac integral of order s, $\eta_F = (E_D - E_F)/\kappa_B T$, and λ is the mean free path of the carriers in the graphene. The prefactor $\alpha \geq 1$ captures the effect of subunity transmission probability between the source/drain metal and the underlying graphene [34]. To calculate R shown in Fig. 7(b) and (c), η_F is obtained from the simulations, while $s = 1/2$, $\alpha = 5$, and $\lambda = 10$ nm are used as fitting parameters to match the experimental data. The assumed carrier (electron and hole) lifetime of 0.1 ns for SiC in the simulated results of Fig. 7(b) and (c) was found to best fit the experimental data.

The symmetric ambipolar $R - V_{\rm bg}$ in Fig. 7(b) shows a good match between the experiment and the model, where $v_{\rm inj} = 10^{-3}$cm/s is assumed for both the electrons and the holes. The Dirac point for the experimental data is shifted to $V_{\rm bg} \approx -3$ V, which might correspond to the presence of charged impurities in the graphene or the surface defects at the graphene/SiC interface (these effects are not incorporated in our simulation). The $R - V_{\rm bg}$ data in Fig. 7(c), on the other hand, show an asymmetric ambipolar dependence of R on the polarity of $V_{\rm bg}$. The origin of the asymmetry is yet to be interpreted in terms of the substrate's photoinduced field effect. We propose that the asymmetry arises from a difference in the magnitude of $v_{\rm inj}$ between the electrons and the holes. A different $v_{\rm inj}$ for electrons and holes would correspond to a mismatch in the effective energy barrier at the graphene/SiC interface for the two carriers according to (1). The dissimilarity in $v_{\rm inj}$ implies a polarity dependence for the density of accumulated carriers at the graphene/Si interface and the corresponding electrostatic doping in graphene, as shown in Figs. 2 and 5. This according to (2) could result in an asymmetric ambipolar $R - V_{\rm bg}$ behavior, as shown in Fig. 7(c). For the simulated result in Fig. 7(c), a relatively small dissimilarity in $v_{\rm inj}$ for the electrons and holes (5×10^{-2} cm/s and 10^{-1} cm/s, respectively) provides a good match with the asymmetric behavior of R versus $V_{\rm bg}$ in the experimental data. In Fig. 7(b) and (c), a sharp rise in the simulated resistance in the vicinity of $V_{\rm bg} = 0$ V corresponds to zero density of states near the Dirac energy in the graphene. Such behavior is not observed in the experimental results probably due to the presence of spatial fluctuations or charge puddles resulting in a finite density of states and energy band broadening in graphene as E_F approaches the Dirac point [25]. The simulation model, by construction, does not account for these nonidealities.

In practice, the calculation of graphene resistance in the phototransistor may involve other considerations beyond the simple approach used in (2). For example, an opposite polarity (or unequal magnitude) of doping in the contact and the channel regions of graphene may exist requiring to consider the transport through p–n (or n–n and p–p) junctions across the graphene layer. The simple approach given by (2), however, provides a first-order comparison between the model and the experiment, while rigorous models could be considered as a part of future studies.

IV. Conclusion

We have developed a computational model for the physical origin of photoresponsivity in graphene phototransistors that are fabricated on an undoped substrate. We showed that the photoresponse is due to the electrostatic doping of the graphene channel induced by the accumulation of photogenerated carriers at the graphene/substrate interface. The accumulation of the charge density strongly depends on the injection velocity (transfer rate) of carrier between the graphene and the substrate. The injection velocity physically depends on the graphene/substrate energy barrier and needs to be significantly smaller than the thermal velocity of carriers to enable a substantial photoresponse. The graphene at the source/drain metal contacts could be electrostatically doped if the relative strength of graphene to contact capacitance is weaker compared with the graphene quantum capacitance. These findings provide important guidelines to optimize the material/interfaces in graphene phototransistors for improving performance/cost. The high photoresponsivity for graphene

phototransistor requires a careful design of the graphene–substrate interface and graphene–metal contacts, e.g., through engineering of thin interfacial oxides and selection of different metals. In addition, different substrate materials could be explored as the photoabsorber layer to optimize cost and the bandwidth of the photoresponse. Finally, the physics of graphene phototransistor, in principle, invites opportunities to explore other 2-D materials besides graphene in a similar device configuration for low-cost/high-performance photodetectors.

APPENDIX

A. Simulation Details

The 2-D numerical simulations under illumination and in dark are performed in a semiclassical simulation tool called PADRE developed at Bell Labs [35]. The coupled set of electrostatics (Poisson) and carrier continuity equations is solved as a function of the applied back-gate voltage ($V_{\rm bg}$). The carrier transport is treated in the drift-diffusion formalism. The Poisson equation is given by

$$\nabla^2 V(x, y) = \frac{q}{\epsilon_{\rm si}}[N_D - N_A + p(x, y) - n(x, y)] \qquad \text{(A1)}$$

where N_D and N_A are the donor and the acceptor doping density, respectively, and p and n are the position-dependent hole and electron density, respectively. The steady-state carrier continuity equation is given as

$$D\frac{\partial^2 n}{\partial x^2} + \mu\varepsilon(x, y)\frac{\partial n}{\partial x} + G(x, y) - R(x, y) = 0 \qquad \text{(A2)}$$

$$D\frac{\partial^2 p}{\partial x^2} - \mu\varepsilon(x, y)\frac{\partial p}{\partial x} + G(x, y) - R(x, y) = 0 \qquad \text{(A3)}$$

where G and R are the carrier generation and recombination rates, respectively, and μ and D are the carrier mobility and diffusion constant, respectively. The carrier generation rate is calculated from the incident power density of the photons and the absorption coefficient (α) in SiC using $G(x, \lambda) = \alpha(\lambda)\varphi(\lambda)e^{-\alpha(\lambda)x}$ [29], where $\varphi(\lambda) = P_{\rm inc}/E_{\rm ph}$ is the incident flux and energy of the incident photons, respectively, at wavelength (λ).

A 500-μm-thick intrinsic SiC substrate acts as the photoabsorber layer having a back metal gate at the bottom and graphene on the top. The bandgap and electron affinity for SiC are 2.9 and 3.3 eV, respectively [31]. For simplicity, the carrier mobility and recombination lifetime in the SiC substrate are assumed to be the same for electrons and holes. The values of 100 cm^2/(V$\cdot$s) and 0.1 μs are used for the mobility and recombination lifetime (except for Fig. 6, as specified in Section III-D), respectively, which are close to the experimentally reported values for 6H–SiC [32], [36]. The channel length is maintained at 1.5 μm. A neutral contact is assumed for the back-gate contact, while the work function of the front metal electrodes is kept the same as for graphene. For undoped graphene, we have used work function of 4.75 eV [37]. In all simulations, source/drain potentials are assumed to be at the ground. The device is illuminated with a monochromatic light at a wavelength of 400 nm. The absorption coefficient of 40/cm is used for the SiC [38].

REFERENCES

[1] A. K. Geim and K. S. Novoselov, "The rise of graphene," *Nature Mater.*, vol. 6, no. 3, pp. 183–191, 2007.

[2] K. S. Novoselov *et al.*, "Two-dimensional gas of massless Dirac fermions in graphene," *Nature*, vol. 438, pp. 197–200, Sep. 2005.

[3] A. H. C. Neto, F. Guinea, N. M. R. Peres, K. S. Novoselov, and A. K. Geim, "The electronic properties of graphene," *Rev. Modern Phys.*, vol. 81, p. 109, Jan. 2009.

[4] K. S. Novoselov *et al.*, "Electric field effect in atomically thin carbon films," *Science*, vol. 306, no. 5696, pp. 666–669, 2004.

[5] F. Schwierz, "Graphene transistors," *Nature Nanotechnol.*, vol. 5, no. 7, pp. 487–496, 2010.

[6] K. S. Novoselov, V. I. Fal'ko, L. Colombo, P. R. Gellert, M. G. Schwab, and K. Kim, "A roadmap for graphene," *Nature*, vol. 490, pp. 192–200, Oct. 2012.

[7] F. Schedin *et al.*, "Detection of individual gas molecules adsorbed on graphene," *Nature Mater.*, vol. 6, no. 9, pp. 652–655, 2007.

[8] F. Bonaccorso, Z. Sun, T. Hasan, and A. C. Ferrari, "Graphene photonics and optoelectronics," *Nature Photon.*, vol. 4, no. 9, pp. 611–622, 2010.

[9] F. Xia, T. Mueller, Y.-M. Lin, A. Valdes-Garcia, and P. Avouris, "Ultrafast graphene photodetector," *Nature Nanotechnol.*, vol. 4, no. 12, pp. 839–843, 2009.

[10] T. Mueller, F. Xia, and P. Avouris, "Graphene photodetectors for high-speed optical communications," *Nature Photon.*, vol. 4, no. 5, pp. 297–301, 2010.

[11] A. Pospischil *et al.*, "CMOS-compatible graphene photodetector covering all optical communication bands," *Nature Photon.*, vol. 7, no. 11, pp. 892–896, 2013.

[12] L. Vicarelli *et al.*, "Graphene field-effect transistors as room-temperature terahertz detectors," *Nature Mater.*, vol. 11, no. 10, pp. 865–871, 2012.

[13] J. Li, L. Niu, Z. Zheng, and F. Yan, "Photosensitive graphene transistors," *Adv. Mater.*, vol. 26, no. 31, pp. 5239–5273, 2014.

[14] Z. Sun and H. Chang, "Graphene and graphene-like two-dimensional materials in photodetection: Mechanisms and methodology," *ACS Nano*, vol. 8, no. 5, pp. 4133–4156, 2014.

[15] F. Liu and S. Kar, "Quantum carrier reinvestment-induced ultrahigh and broadband photocurrent responses in graphene–silicon junctions," *ACS Nano*, vol. 8, no. 10, pp. 10270–10279, 2014.

[16] M. Freitag, T. Low, and P. Avouris, "Increased responsivity of suspended graphene photodetectors," *Nano Lett.*, vol. 13, no. 4, pp. 1644–1648, 2013.

[17] G. Konstantatos *et al.*, "Hybrid graphene–quantum dot phototransistors with ultrahigh gain," *Nature Nanotechnol.*, vol. 7, no. 6, pp. 363–368, 2012.

[18] Y. Zhang *et al.*, "Broadband high photoresponse from pure monolayer graphene photodetector," *Nature Commun.*, vol. 4, p. 1811, May 2013.

[19] Y. Liu *et al.*, "Plasmon resonance enhanced multicolour photodetection by graphene," *Nature Commun.*, vol. 2, p. 579, Dec. 2011.

[20] X. Gan *et al.*, "Chip-integrated ultrafast graphene photodetector with high responsivity," *Nature Photon.*, vol. 7, no. 11, pp. 883–887, 2013.

[21] M. Foxe *et al.*, "Detection of ionizing radiation using graphene field effect transistors," *IEEE Trans. Nanotechnol.*, vol. 581, p. 11, 2012.

[22] B. K. Sarker, I. Childres, E. Cazalas, I. Jovanovic, and Y. P. Chen, "Tunable photocurrent and photoresponsivity of graphene/silicon carbide field effect photodetectors," in *Proc. APS Meeting Abstracts*, vol. 1. 2014.

[23] E. Cazalas, I. Childres, A. Majcher, T.-F. Chung, Y. P. Chen, and I. Jovanovic, "Hysteretic response of chemical vapor deposition graphene field effect transistors on SiC substrates," *Appl. Phys. Lett.*, vol. 103, no. 5, p. 053123, 2013.

[24] B. K. Sarker, I. Childres, E. Cazalas, I. Jovanovic, and Y. P. Chen. (2014). "Gate-tunable and high responsivity graphene phototransistors on undoped semiconductor substrates." [Online]. Available: http://arxiv.org/abs/1409.5725

[25] D. Berdebes, T. Low, Y. Sui, J. Appenzeller, and M. S. Lundstrom, "Substrate gating of contact resistance in graphene transistors," *IEEE Trans. Electron Devices*, vol. 58, no. 11, pp. 3925–3932, Nov. 2011.

[26] M. Vanin, J. J. Mortensen, A. K. Kelkkanen, J. M. Garcia-Lastra, K. S. Thygesen, and K. W. Jacobsen, "Graphene on metals: A van der Waals density functional study," *Phys. Rev. B*, vol. 81, p. 081408, Feb. 2010.

[27] C. R. S. da Silva, J. F. Justo, and I. Pereyra, "Crystalline silicon oxycarbide: Is there a native oxide for silicon carbide?" *Appl. Phys. Lett.*, vol. 84, no. 24, pp. 4845–4847, 2004.

[28] F. Amy, P. Soukiassian, Y. K. Hwu, and C. Brylinski, "Si-rich 6H- and 4H–SiC(0001) 3×3 surface oxidation and initial SiO_2/SiC interface formation from 25 to 650 °C," *Phys. Rev. B*, vol. 65, p. 165323, Apr. 2002.
[29] S. M. Sze and K. K. Ng, *Physics of Semiconductor Devices*. New York, NY, USA: Wiley, 2006.
[30] S. Datta, "Nanoscale device modeling: The Green's function method," *Superlattices Microstruct.*, vol. 28, no. 4, pp. 253–278, 2000.
[31] M. E. Levinshtein, S. L. Rumyantsev, and M. S. Shur, *Properties of Advanced Semiconductor Materials: GaN, AIN, InN, BN, SiC, SiGe*. New York, NY, USA: Wiley, 2001.
[32] C. F. Zhe, *Silicon Carbide: Materials, Processing and Devices*, vol. 20. Boca Raton, FL, USA: CRC Press, 2003.
[33] M. Lundstrom, T. Low, and D. Berdebes. *Low Bias Transport in Graphene: An Introduction (Lecture Notes)*. [Online]. Available: https://nanohub.org/resources/7435
[34] F. Xia, V. Perebeinos, Y.-M. Lin, Y. Wu, and P. Avouris, "The origins and limits of metal–graphene junction resistance," *Nature Nanotechnol.*, vol. 6, pp. 179–184, 2011.
[35] M. R. Pinto *et al. Padre*. [Online]. Available: https://nanohub.org/resources/padre
[36] M. Roschke and F. Schwierz, "Electron mobility models for 4H, 6H, and 3C SiC [MESFETs]," *IEEE Trans. Electron Devices*, vol. 48, no. 7, pp. 1442–1447, Jul. 2001.
[37] Y.-J. Yu, Y. Zhao, S. Ryu, L. E. Brus, K. S. Kim, and P. Kim, "Tuning the graphene work function by electric field effect," *Nano Lett.*, vol. 9, no. 10, pp. 3430–3434, 2009.
[38] R. Groth and E. Kauer, "Absorption freier Ladungsträger in α-SiC-kristallen," *Phys. Status Solidi B*, vol. 1, no. 5, pp. 445–450, 1961.

Nauman Zafar Butt received the B.S. degree in electrical engineering from the University of Engineering and Technology, Lahore, Pakistan, and the Ph.D. degree in electrical engineering from Purdue University, West Lafayette, IN, USA, in 2008,

He was with the IBM Semiconductor Research and Development Center, East Fishkill, NY, USA, till 2012. He joined the Department of Electrical Engineering, Lahore University of Management Sciences, Lahore, in 2013, as an Assistant Professor.

Biddut Sarker received the Ph.D. degree in physics from the University of Central Florida, Orlando, FL, USA, in 2012.

He is currently a Post-Doctoral Research Associate with the Birck Nanotechnology Center and the Department of Physics and Astronomy, Purdue University, West Lafayette, IN, USA.

Yong P. Chen received the M.Sc. degree in mathematics from the Massachusetts Institute of Technology, Cambridge, MA, USA, and the Ph.D. degree in electrical engineering from Princeton University, Princeton, NJ, USA.

He is currently an Associate Professor of Physics and Astronomy and Electrical and Computer Engineering with Purdue University, West Lafayette, IN, USA.

Muhammad Ashraful Alam (M'96–SM'01–F'06) received the Ph.D. degree in electrical engineering from Purdue University, West Lafayette, IN, USA, in 1995.

After spending a decade in Bell Laboratories in Murray Hill, NJ, he joined Purdue University in 2004, where he is currently the J. N. Gupta Professor of Electrical Engineering. His current research interests include physics, performance limits, and novel concepts in classical and emerging electronic devices.